

Article

Utilizing a Long Short-Term Memory Algorithm Modified by Dwarf Mongoose Optimization to Predict Thermal Expansion of Cu-Al₂O₃ Nanocomposites

Ayman M. Sadoun ^{1,*} , Ismail R. Najjar ¹, Ghazi S. Alsuruji ¹, Ahmed Wagih ² and Mohamed Abd Elaziz ^{3,4,5} 

¹ Mechanical Engineering Department, Faculty of Engineering, King Abdulaziz University, Jeddah 80204, Saudi Arabia; inajjar@kau.edu.sa (I.R.N.); ghazigo@hotmail.com (G.S.A.)

² Department of Mechanical Design and Production Engineering, Faculty of Engineering, Zagazig University, Zagazig 44519, Egypt; eng_awa2011@yahoo.com

³ Faculty of Computer Science & Engineering, Galala University, Suze 43511, Egypt; abd_el_aziz_m@yahoo.com

⁴ Artificial Intelligence Science Program, Faculty of Science & Engineering, Galala University, Suze 43511, Egypt

⁵ Department of Mathematics, Faculty of Science, Zagazig University, Zagazig 44519, Egypt

* Correspondence: assadoun@kau.edu.sa

Abstract: This paper presents a machine learning model to predict the effect of Al₂O₃ nanoparticle content on the coefficient of thermal expansion in Cu-Al₂O₃ nanocomposites prepared using an in situ chemical technique. The model developed is a modification of Long Short-Term Memory (LSTM) using dwarf mongoose optimization (DMO), which mimics the behavior of DMO to find its food for predicting the behavior of the composite. The swarm of DMO consists of three groups, namely the alpha group, scouts, and babysitters. Each group has its own behavior to capture the food. The preparation of the nanocomposite was performed using aluminum nitrate that was added to a solution containing scattered copper nitrate. After that, the powders of CuO and Al₂O₃ were obtained, and the leftover liquid was removed using thermal treatment at 850 °C for 1 h. The powders were consolidated using compaction and sintering processes. The impact of Al₂O₃ contents on the thermal properties of the Cu-Al₂O₃ nanocomposite was investigated. The results showed that the Thermal Expansion Coefficient (TEC) decreases with increasing Al₂O₃ content due to the increased precipitation of Al₂O₃ nanoparticles at the grain boundaries of the Cu matrix. Moreover, the good interfacial bonding between Al₂O₃ and the Cu may participate in this decrease in TEC. The proposed machine learning model was able to predict the TEC of all the produced composites with different Al₂O₃ content and was tested at different temperatures with very good accuracy, reaching 99%.

Keywords: metal matrix nanocomposites; thermal properties; artificial neural network; dwarf mongoose optimization (DMO); long short-term memory (LSTM)

MSC: 70



Citation: Sadoun, A.M.; Najjar, I.R.; Alsuruji, G.S.; Wagih, A.; Abd Elaziz, M. Utilizing a Long Short-Term Memory Algorithm Modified by Dwarf Mongoose Optimization to Predict Thermal Expansion of Cu-Al₂O₃ Nanocomposites. *Mathematics* **2022**, *10*, 1050. <https://doi.org/10.3390/math10071050>

Academic Editor: Paul W. Eloe

Received: 3 March 2022

Accepted: 23 March 2022

Published: 24 March 2022

Publisher's Note: MDPI stays neutral with regard to jurisdictional claims in published maps and institutional affiliations.



Copyright: © 2022 by the authors. Licensee MDPI, Basel, Switzerland. This article is an open access article distributed under the terms and conditions of the Creative Commons Attribution (CC BY) license (<https://creativecommons.org/licenses/by/4.0/>).

1. Introduction

Metal matrix nanocomposites are a new class of material with a high chance of success in many applications due to outstanding composite properties such as good mechanical strength and better creep resistance at elevated temperatures [1–3]. A combination of the metal matrix with nano-sized ceramic reinforcement has been characterized as a well-accepted description of metal matrix composites [4,5]. Copper and its alloys are used in applications where good wear resistance and high thermal and electrical conductivity are required, such as electrical connectors, sliding contacts, and integrated circuit sealing materials [6–10]. However, the highest coefficient of friction, low wear resistance, and strength reduced its application in heavy-duty applications.

To tackle this problem, research has been carried out to manufacture copper-based composites with high electrical and thermal conductivity, while retaining good strength, hardness, and wear behavior at elevated temperatures. Ceramic particles dispersion-strengthened copper, on the other hand, can maintain its strength at high temperatures [11,12]. Copper matrix composites with oxide dispersion strengthening (ODS) have better electrical and thermal conductivity, as well as improved yield strength and wear resistance. Even when heated to temperatures near the melting point of the metal matrix, the oxides rarely dissolve, and dispersion strengthening of composites can be sustained [13].

The researchers tried to tackle these problems by immersing ceramic particles in the Cu-matrix to improve thermal properties, such as adding Al_2O_3 [14,15], SiC [16], Graphene [17–19], ZrO_2 [20–23], and WC [24,25] to it to provide a new material with a combination of metal and ceramic properties. A nanocomposite can improve mechanical, optical, magnetic, and thermal properties, making it useful in industries such as aerospace, automotive, electronics, sensors, catalysts, marine, chemical, biomaterials, and energy storage and conversion. The hardness or microhardness, wear, and corrosion resistance of Ni- Al_2O_3 , Cu- Al_2O_3 [26–29], and Ni- TiO_2 [30] metal matrix composites (MMCs) are found to be superior to the bare substrate. Hardness increased as the space between particles shrank, preventing dislocation movement and allowing more nanoparticles to be incorporated.

Powder metallurgy is one of the best techniques to manufacture metal matrix nanocomposites due to its low cost [31–34]. Despite this important advantage for the industry, the low dispersion of the reinforcement phase in the matrix limits its applicability. Researchers have recently employed in situ chemical processes to manufacture nanocomposite materials by employing the casting process to mix the nanoparticle reinforcement directly with the melted matrix [35–38]. They discovered that using this procedure improved the characteristics because there was no considerable agglomeration and effective distribution of nanoparticles occurred in the melt. Sadoun et al. [39] explored how alumina-coated silver particles affected the electrochemical performance and corrosion resistance of Cu- Al_2O_3 nanocomposites made via powder metallurgy. According to their findings, the relative density fell as the amount of Al_2O_3 rose, and the corrosion rate decreased until 9% Al_2O_3 reinforcement but increased thereafter. Rodrigues et al. [40] manufactured a Cu- Al_2O_3 /graphene nanocomposite using a milling process for electromechanical applications. They reported that electrical and thermal stability was achieved after 4 h of milling. Additionally, the wear and mechanical properties of the produced composite were improved compared to unreinforced metal.

Owing to the advantages of artificial intelligence in providing solutions for very complex problems regardless of the availability of labs and the cost, it was deployed to predict the coefficient of thermal expansion of Cu- Al_2O_3 nanocomposites [41–44]. We trained the newly developed Long Short-Term Memory (LSTM) using experimental data obtained from abrasive wear tests to predict the response of these nanocomposites with different Al_2O_3 content with good accuracy.

In this work, thermal expansion and thermal conductivity are the most important properties of Cu and its composite and allow applications in many thermal and electrical fields. Here, we investigate the effect of Al_2O_3 nanoparticles on the thermal properties of Cu-based nanocomposites. We deployed an in situ chemical method to manufacture Cu- Al_2O_3 nanocomposites with different Al_2O_3 content. The microstructure and thermal properties of the produced nanocomposites were characterized. Moreover, we developed Long Short-Term Memory (LSTM) to predict the coefficient of thermal expansion of the produced nanocomposites. This modification of LSTM depends on using a new meta-heuristic technique, named dwarf mongoose optimization (DMO) [45], which is used to determine the parameters of LSTM to find the best configuration. The main motivation behind using DMO is its ability to balance the exploration and exploitation during the search process of the feasible region and optimal solution. In addition, it has been applied to different global and engineering optimization problems. According to the obtained results, DMO established its efficiency in solving problems better than competitive algorithms.

The proposed algorithm was trained using 70% of the experimental results obtained from composites with different Al₂O₃ content tested at different temperatures, while the other 30% of the data were used to test it. The development of these composites with optimum thermal expansion combined with good mechanical and wear properties will increase their applicability in thermal applications such as heat sinks.

2. Machine Learning Models

In this section, we present the basic concepts of Long Short-term Memory, Dwarf Mongoose Optimization (DMO), and the proposed model.

2.1. Long Short-Term Memory

Long Short-term Memory (LSTM) [1] is a gradient-based recurrent neural network architecture that solves typical recurrent neural networks' vanishing gradient problems. Long-term dependencies in texts are a problem that develops during the training phase of a conventional RNN when backpropagation through the time gradient descent tends to evaporate, or in rare situations, explode exponentially.

Because of its architecture, as illustrated in Figure 1, LSTM is able to properly manage long-term dependencies in the text. This architecture allows it to store information for long periods of time, which is something that the normal RNN struggles with. The LSTM network is made up of a series of recurrently connected memory cells that use the idea of gating, which is a technique that adds or removes information to control the cell state of each individual memory cell [2]. Each LSTM is made up of three gates: Input, forget, and output. Each gate is made up of a sigmoid neural network layer and a pointwise multiplication operation.

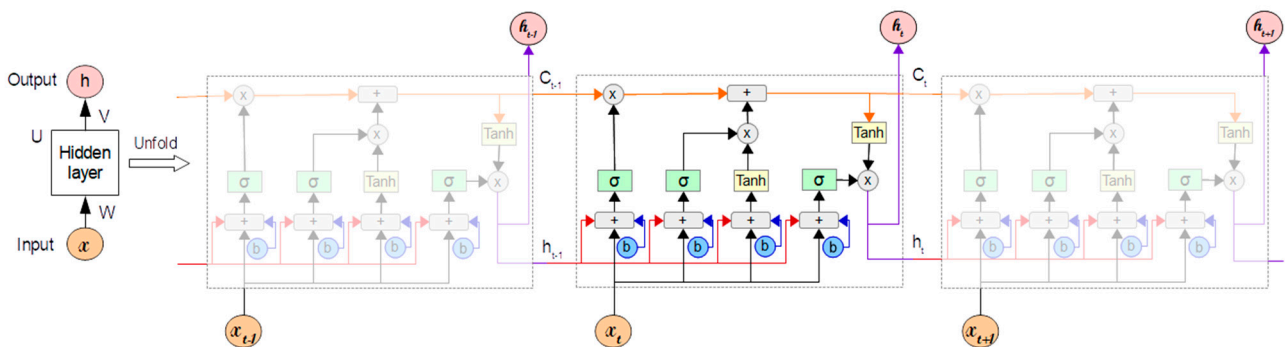


Figure 1. Long Short-Term Memory neural network structure.

Using X as the input vector at time t and N as the number of LSTM cells in the forward pass, the input from the current state and the hidden state of the previous cell is first passed to the forget gate, as shown in Figure 1, to determine whether to store the information with an output of 1 or discard it with an output of 0 (Equation (1)). The fundamental purpose of forget gates is to decide whether or not to forget the knowledge. The sigmoid activation function output (σ) of the sum of the bias (b_f) and the product between the weights (W_f) and the inputs (h_{t-1}, X_t), which comprises the input from the previous state (h_{t-1}) and the current input (X_t), is the forget value (f_t), which is between zero and one.

$$f_t = \sigma(W_f \cdot [h_{t-1}, X_t] + b_f) \tag{1}$$

The next step is to use the update of the cell state (C_t) using the following equation

$$C_t = C_{t-1} \cdot f_t + N_t \cdot i_t \tag{2}$$

where N_t represents the output of the tanh function, which uses W_n, h_{t-1}, X_t , and b_n , and this formulated as

$$N_t = \tanh(W_n \cdot [h_{t-1}, X_t] + b_n) \tag{3}$$

In Equation (2), i_t refers to the output of the sigmoid layer defined as:

$$i_t = \sigma(W_i \cdot [h_{t-1}, X_t] + b_i) \tag{4}$$

Thereafter, the sigmoid activation output (O_t) is computed using Equation (5) and depends on the current input (X_t), previous state (h_{t-1}), weights (W_o), and bias (b_o).

$$O_t = \sigma(W_o \cdot [h_{t-1}, X_t] + b_o) \tag{5}$$

The next process is to update the hidden state (h_t) using Equation (6).

$$h_t = O_t \cdot \tanh(C_t) \tag{6}$$

2.2. Dwarf Mongoose Optimization Algorithm

In this section, the mathematical model of Dwarf Mongoose Optimization (DMO) is introduced [45]. This algorithm simulates the behavior of the dwarf mongoose when finding its food. In general, DMO begins by setting the initial value for a set of solutions using the following formula:

$$x_{i,j} = l_j + rand \times (u_j - l_j) \tag{7}$$

where *rand* is a random number generated from [0,1]. u_j and l_j are the limits of the search domain. The swarm of DMO consists of three groups, namely the alpha group, scouts, and babysitters. Each group has its own behavior to capture the food, and the details of these groups are given as follows:

2.2.1. Alpha Group

The fitness of each solution is computed once the population has been initiated. Equation (8) calculates the likelihood value for each population fitness, and the alpha female (α) is chosen based on this probability.

$$\alpha = \frac{fit_i}{\sum_{i=1}^n fit_i} \tag{8}$$

n corresponds to the number of mongooses in the alpha group. The number of babysitters is denoted by *bs*. *Peep* is the vocalisation of the dominant female that keeps the family on track.

Each mongoose sleeps in the first sleeping mound, which is set to \emptyset . The DMO employs the expression in Equation (4) to generate a candidate food position.

$$X_{i+1} = X_i + phi \times peep \tag{9}$$

The sleeping mound is provided in Equation (10) after each repetition, where *phi* is a uniformly distributed random value [-1,1].

$$sm_i = \frac{fit_{i+1} - fit_i}{\max\{|fit_{i+1}, fit_i|\}} \tag{10}$$

Equation (11) contains the average value of the sleeping mound.

$$\varphi = \frac{\sum_{i=1}^n sm_i}{n} \tag{11}$$

Once the babysitting exchange criterion is met, the algorithm advances to the scouting phase, where the next food source or sleeping mound is considered.

2.2.2. Scout Group

Because mongooses are known to not return to past sleeping mounds, the scouts look for the next sleeping mound, ensuring exploration. For our model, scouting and foraging are performed at the same time, as explained in [36]. This movement is modeled after a successful or unsuccessful search for a new sleeping mound. In other words, the migration of the mongooses is contingent on their total performance. The reasoning for this is that if the family forages far enough, they will come to a new sleeping mound. The scout mongoose is represented by Equation (12).

$$X_{i+1} = \begin{cases} X_i - CF * phi * rand * [X_i - \vec{M}] & \text{if } \varphi_{i+1} > \varphi_i \\ X_i + CF * phi * rand * [X_i - \vec{M}] & \end{cases} \quad (12)$$

where *rand* exemplifies an arbitrary number in the range [0, 1], $CF = \left(1 - \frac{iter}{Max_{iter}}\right)^{\left(2 \frac{iter}{Max_{iter}}\right)}$ where the parameter that regulates the mongoose group’s collective-volitive movement is decreased linearly as the iterations progress. $\vec{M} = \sum_{i=1}^n \frac{X_i \times sm_i}{X_i}$ where the mongoose’s movement to the new sleeping mound is determined by this vector.

2.2.3. Babysitters Group

Babysitters are usually inferior group members that stay with the young and are cycled on a regular basis to allow the alpha female (mother) to lead the rest of the group on daily foraging expeditions. She usually comes back to milk the young in the afternoon and evening. The number of babysitters is proportional to the size of the population; they influence the algorithm by reducing the total population size based on the percentage set. By lowering the population size by the percentage of babysitters, we may replicate this group. The scouting and food source information previously held by the family members replacing them is reset using the babysitter exchange parameter. The babysitters’ fitness weight is set to zero, ensuring that the alpha group’s average weight is reduced in the next iteration, obstructing group movement and intensifying exploitation. Algorithm A1 contains the pseudocode for the suggested algorithm (see Appendix A).

2.3. Proposed Model

The steps of the prediction thermal model are given in Figure 2. In general, the presented model, named LSTM-DMO, depends on using the behavior of the DMO algorithm to determine the parameters of the LSTM network.

The first step in LSTM-DMO is to form the initial solutions, which represent the value of each parameter of LSTM using the following equation:

$$X_{ij} = l_j + r \times (u_j - l_j), \quad i = 1, \dots, N, \quad j = 1, \dots, D, \quad r \in [0, 1] \quad (13)$$

In Equation (13), u_j and l_j represent the boundaries of each parameter of LSTM, whereas D refers to the number of parameters in X_i . We set $D = 5$ since there are five parameters that need to be determined, which include Max Epochs (Max_E), the optimization method (Op_M), the Minimum Batch Size (B_S), the Learn Rate Drop Factor (LRD_F), and the number of Hidden Units (N_h). In addition, $Op_M \in \{1, 2, 3\}$ represents the stochastic gradient descent with momentum (SGDM), RMSProp, and Adam optimizer, respectively. $N_h \in [20, 200]$, $LRD_F \in [0.1, 0.9]$, $Max_E \in [20, 300]$, and $B_S \in [64, 265]$. For clarity, let $X_i = [Max_E, Op_M, B_S, LRD_F, N_h] = [150, 2, 30, 0.4, 50]$, which means that RMSProp is used as the optimization algorithm with $Max_E = 100$, $LRD_F = 0.4$, $N_h = 50$, $B_S = 30$. From this example, it can be observed that the DMO algorithm is modified to deal with mixed values (i.e., integral and decimal), and this is not included in the original implementation of DMO.

The next step is to use the following formula as an objective function to assess the performance of output Y_P obtained using the training set, representing 70% of input data, and the current parameters of LSTM X_i .

$$Fit_i = \sqrt{\frac{\sum_{i=1}^{N_s} (Y_P - Y_T)^2}{N_s}} \tag{14}$$

where N_s is the number of cases of the training set with the target Y_T . Thereafter, the best solution is determined, and we use the operators of DMO to update other solutions as in the Equations. This updating stage is conducted until reaching the stop conditions, then returning the best solution. Using the testing set, which represents 30% of the input data, we evaluate the performance of the obtained best solution using performance metrics.

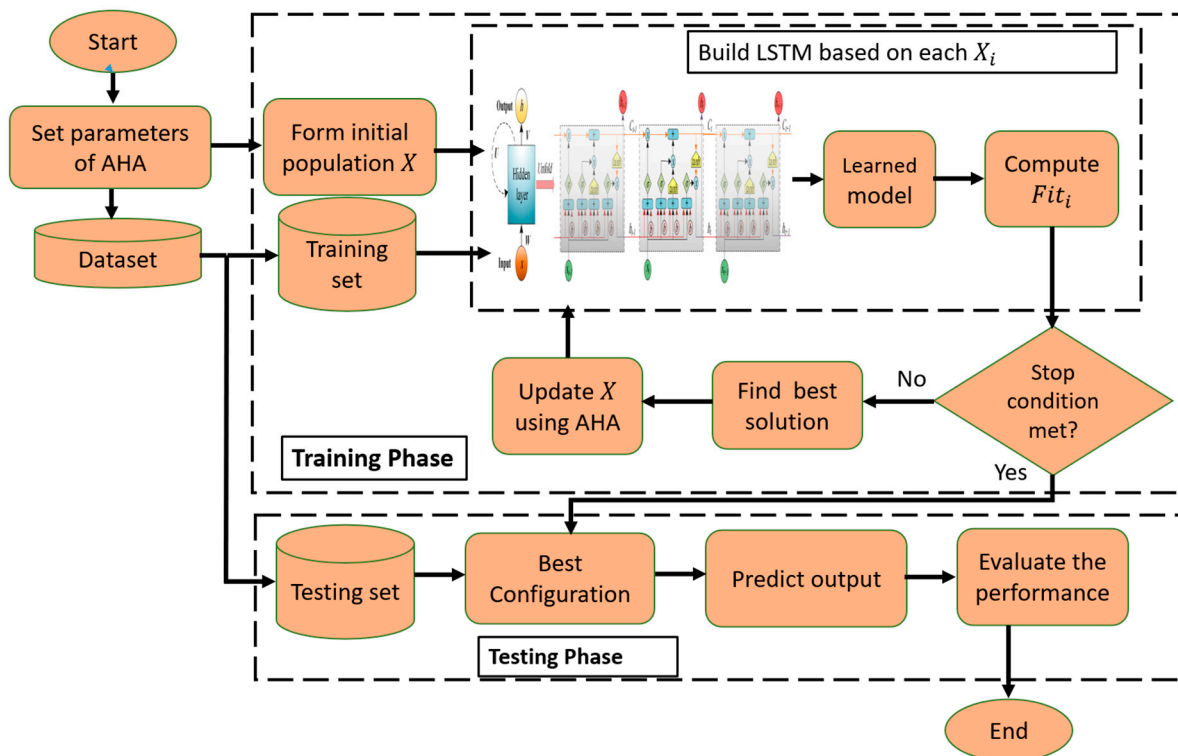


Figure 2. Structure of LSTM-DMO model.

2.4. Prediction of Thermal Expansion Using the Improved LSTM Model

To validate the performance of LSTM-DMO as a prediction model, we use a set of performance metrics including the root mean square error (RMSE), mean absolute error (MAE), and coefficient of determination R^2 . The definition of these metrics is formulated as:

$$R^2 = \frac{\left(\sum_{i=1}^{n_s} (d_i - \bar{d})(y_i - \bar{y})\right)^2}{\sum_{i=1}^{n_s} (d_i - \bar{d})^2 \times \sum_{i=1}^{n_s} (y_i - \bar{y})^2} \tag{15}$$

$$RMSE = \sqrt{\frac{1}{n_s} \sum_{i=1}^{n_s} (d_i - y_i)^2} \tag{16}$$

$$MAE = \frac{1}{n_s} \sum_{i=1}^{n_s} |d_i - y_i| \tag{17}$$

In Equations (15)–(17), n_s , d , y , \bar{d} , and \bar{y} represent the number of testing/training samples, the observed value, the predicted value, the average of observed values, and the average of predicted values, respectively.

3. Experiments

The in situ chemical process was used to synthesize Cu-Al₂O₃ nanocomposite powder from water-soluble copper Cu(NO₃)₂·3H₂O and aluminum nitrates Al(NO₃)₃·9H₂O. The in situ chemical process comprises several steps as Cu(NO₃)₂·3H₂O and Al(NO₃)₃·9H₂O were dissolved in water using a magnetic stirrer at 70 °C for 30 min. The salt concentrations were chosen to produce a Cu-Al₂O₃ nanocomposite system with 2.5, 7.5, and 12.5 wt.% Al₂O₃. Then, to obtain nitrate salt powder precursor particles, dry spraying was performed with a sprayer at 180 °C. Copper oxide (CuO) and aluminum oxide (Al₂O₃) phases were obtained via oxidation of the powder at 850 °C for 1 h in an air atmosphere. Finally, reduction of the powders in hydrogen for 30 min at 500 °C. The reactor was then cooled in a high-purity argon environment to prevent oxidation, with copper oxide reduced to its metallic state and Al₂O₃ remaining as the scattered ceramic phase.

To consolidate the samples, powders were placed inside a steel die and then cold-pressed at a pressure of 700 MPa. Finally, sintering of the compacted samples was performed for 2 h in hydrogen gas at a temperature of 900 °C. The crystal structure and the phase composition of the used powders and the fabricated nanocomposites were identified by X-ray diffraction (XRD) with the model D8 Kristalloflex. We used a Field Emission Scanning Electron Microscope (FE-SEM; QUANTA FEG250) with energy dispersive X-ray (EDX) spectrometers attached to characterize the morphological changes in the powder and consolidated samples. EDX analysis was performed to examine the composition of the fabricated nanocomposites. According to MPIF standards 42, 1998, and using distilled water, the Archimedes method was used to evaluate the densities of the produced samples. The electrical conductivity of the nanocomposites was measured using PHYWE SYSTEME GMBH 37070 Gottingen, Germany. Based on the results of the electrical conductivity, values of the thermal conductivity were determined by the Wiedemann–Franz equation [46].

$$\frac{k}{\sigma} = LT \quad (18)$$

where k is the thermal conductivity (W/mK), σ is the electrical conductivity $\Omega \cdot \text{m}^{-1}$, T is the absolute temperature in degrees Kelvin (293 K), and L is the Lorentz number = $2.44 \times 10^{-8} \text{ W} \cdot \Omega \cdot \text{K}^{-2}$. A digital indicator and electrical furnace were used to measure the coefficient of thermal expansion (CTE). A temperature range between 50 °C and 600 °C was applied with equal heating and cooling rates, 3 °K/min, in an argon atmosphere.

4. Results and Discussion

4.1. Structural and Thermal Properties

Figure 3 shows the morphology of the produced powders with different Al₂O₃ contents after deoxidization. As seen in Figure 3a, the particles cluster together to form large particle groups with an average particle size of less than 200 nm. The generated particles' roughly spherical shape improves wettability throughout the phases [47–51]. The microstructure of solidified composites is influenced by the formation of reinforcing particles. Figure 3c depicts high magnification of the same composite, demonstrating that the particle size after the chemical procedure is nanoscale. The XRD examination of the nanocomposite powder in Figure 3d shows the presence of Cu and Al₂O₃ exclusively, with no other components accumulating throughout the chemical process. This provides proof of the manufacturing process' authenticity as well as the composition of the materials produced.

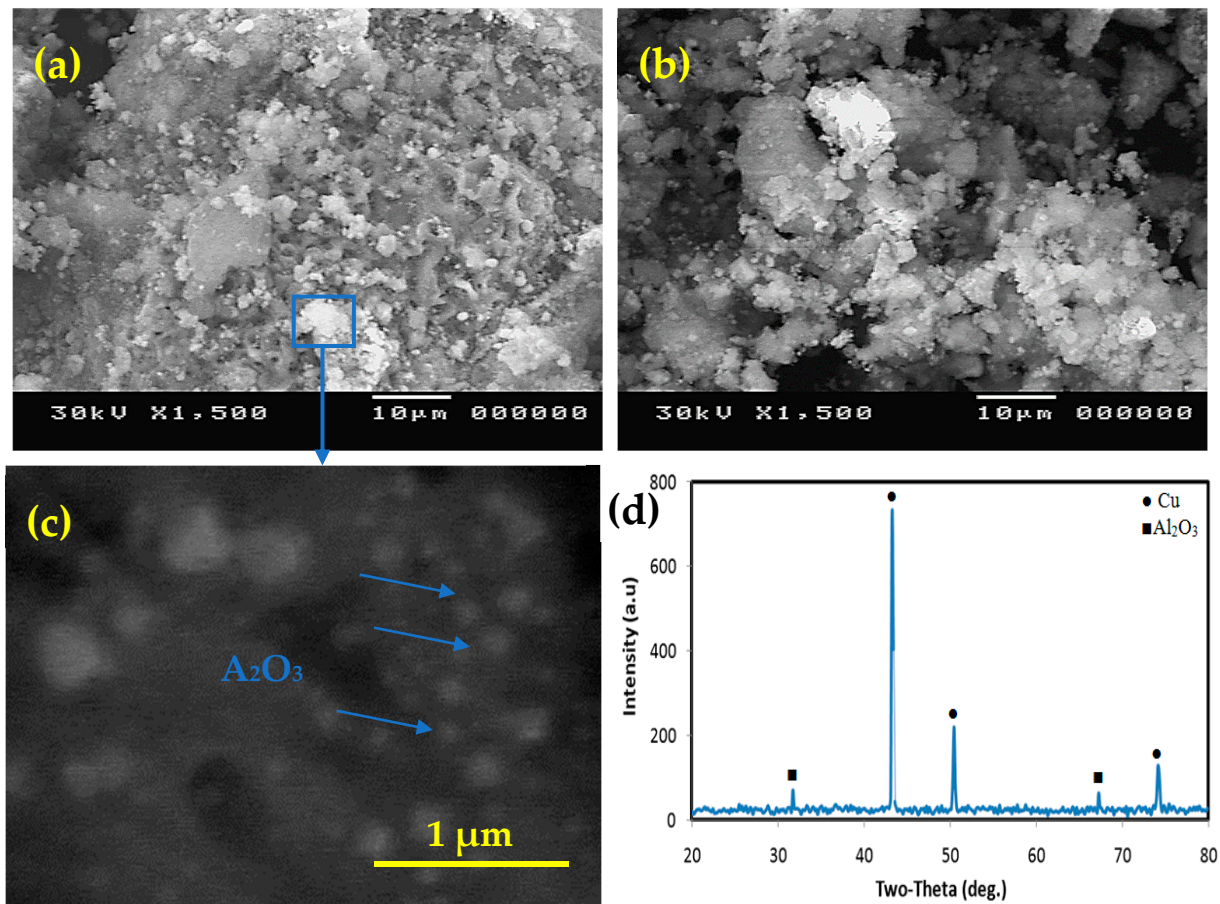


Figure 3. SEM micrograph of the nanocomposite powders; (a) Cu-2.5%Al₂O₃, (b) Cu-12.5%Al₂O₃, (c) enlarged image of the rectangular area marked in (a), (d) XRD of Cu-12.5%Al₂O₃.

Figure 4 shows the morphology of the consolidated Cu-Al₂O₃ nanocomposite with different Al₂O₃ content. The figures generally reflect the good distribution of Al₂O₃ in all samples. The particle and grain sizes of Cu and Al₂O₃ are very small, reaching 100 nm, which makes the grain boundary relatively small around each grain. The presence of grain refinement in the samples is in accordance with the formation of voids as shown in Figure 4. This entrapped air is difficult to extract during sintering due to the good bond between Al₂O₃, resulting in a larger void content. Moreover, the large mismatch between the surface energy of Cu and Al₂O₃ particulates helps in the generation of voids at the interface between Al₂O₃ and Cu. However, this can be a mechanism of void generation. This can only contribute to the micro void formation, which will be clarified in the next subsection. Furthermore, some Al₂O₃ nanoparticles lay at grain boundaries, increasing the size of the grain boundary and improving its properties. The presence of Al₂O₃ at grain boundaries decreases the capacity of grains to re-weld during sintering, resulting in welded grains of a large size, similar to pure metal behavior. As a result, the presence of Al₂O₃ nanoparticles reinforces the grains by penetrating the grains' lamellar structure and laying at the grain borders. The distribution of reinforcement in the matrix is another key element that influences the characteristics of nanocomposites.

Figure 5 shows the mapping analysis of the Cu-12.5%Al₂O₃ nanocomposite with the elemental analysis of each component. The figure reflects the good distribution of the reinforcing phases in this composite with the complete absence of agglomeration at the nanoscale. The elemental analysis demonstrates that the sample's composition is devoid of impurities, with Cu, Al, and O being the only elements discovered in the sample.

Figure 6 shows the relative density measurements of the Cu- Al_2O_3 nanocomposite after the fabrication process. The density of the nanocomposite is decreased by increasing the content of the Al_2O_3 from 94.6 for the sample containing 0.0% Al_2O_3 to 88.2 for the sample containing 12.5% Al_2O_3 . It is well known that reinforcing the matrix with light materials leads to a decrease in the density of the matrix [52,53]. Increasing the ceramic reinforcement percentage, especially that in the nano-size, increases the chance of producing agglomeration that, in turn, leads to a decrease in the density of the matrix.

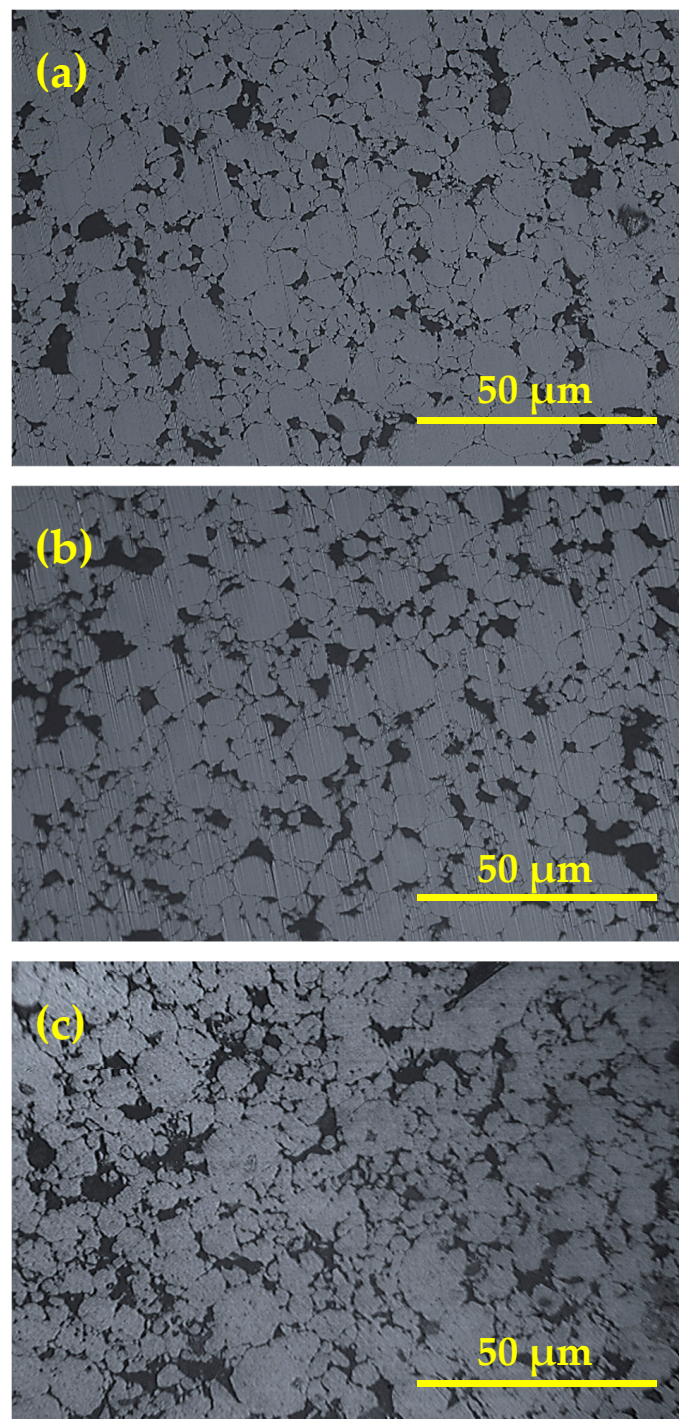


Figure 4. Microstructure of Cu- Al_2O_3 nanocomposites; (a) Cu-2.5% Al_2O_3 , (b) Cu-7.5% Al_2O_3 , (c) Cu-12.5% Al_2O_3 .

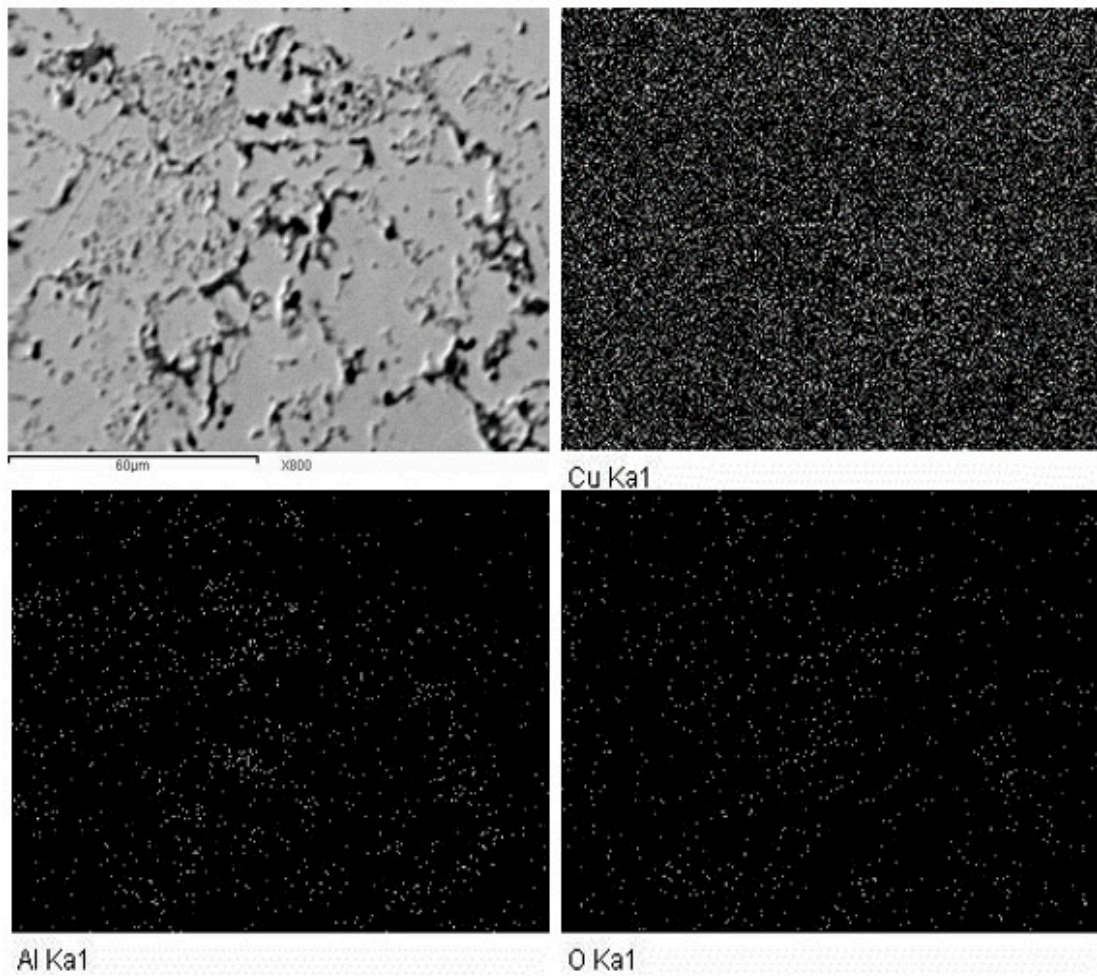


Figure 5. Mapping and EDS analysis of Cu-12.5%Al₂O₃ nanocomposite.

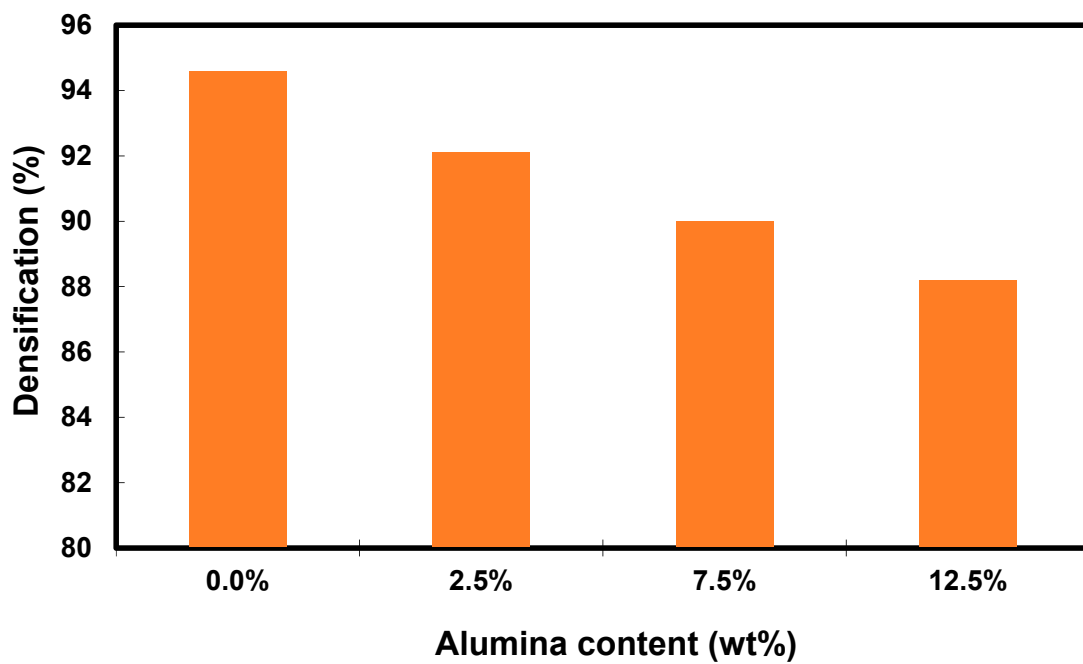


Figure 6. Bar graph of densification of Cu-Al₂O₃ nanocomposites as a function of Al₂O₃ content.

Figure 7 simulates the electrical resistivity of the Cu-Al₂O₃ nanocomposites. The electrical resistivity is proportional to Al₂O₃ addition up to 12.5%, which was observed. As the figure illustrates, the electrical resistivity increases from 2.32×10^{-8} to $6.78 \times 10^{-8} \Omega \cdot m$ for nanocomposites with 0% and 12.5 wt.% Al₂O₃, respectively. Increasing the electrical resistivity of the Cu-Al₂O₃ nanocomposites by increasing the amount of the Al₂O₃ up to 12.5 wt.% Al₂O₃ is attributed to more than one reason. The first reason is the homogeneous distribution of the Al₂O₃ inside the matrix, as shown in Figure 4. The second reason is the good adhesion between the Al₂O₃ and the matrix. Finally, it is related to the remarkable electrical properties of Al₂O₃. Furthermore, the higher porosity content caused by the presence of Al₂O₃ nanoparticles obstructs the free electron movement, increasing the nanocomposite's resistivity over the Cu matrix [54,55].

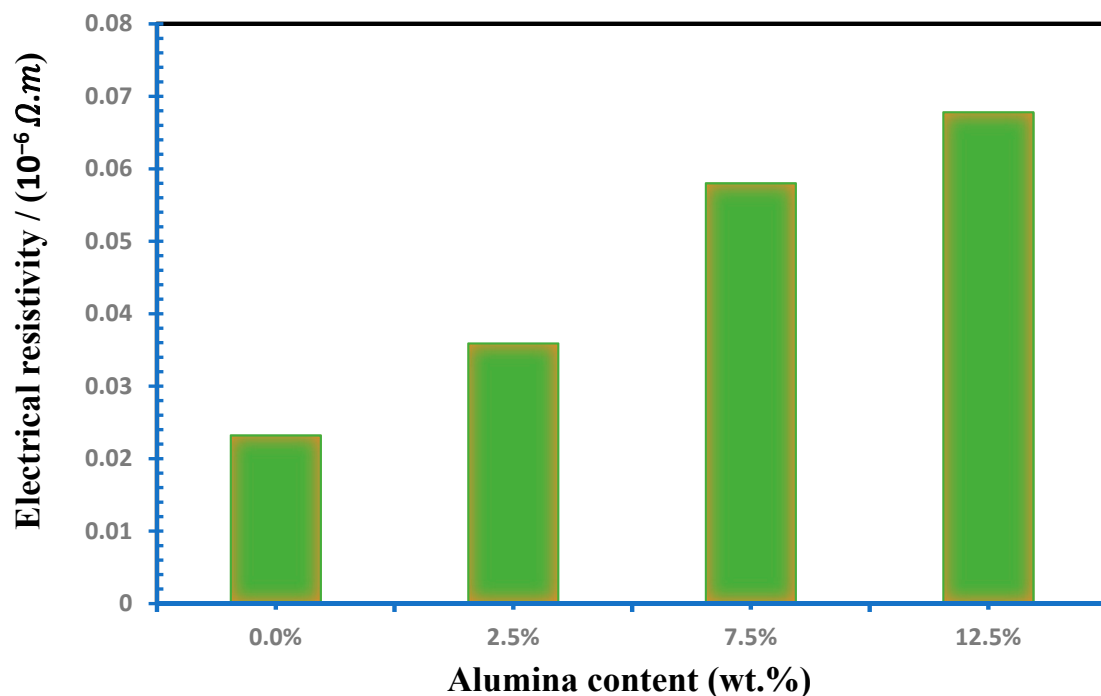


Figure 7. Influence of Al₂O₃ contents on electrical resistivity of Cu-Al₂O₃ nanocomposites.

Figure 8 shows the thermal expansion coefficient (TEC) of the Cu-Al₂O₃ nanocomposites, with its different content of Al₂O₃, as a function of temperature. It is observed that for the different composites considered, the TEC increases as the temperature increases. This is because, as the temperature increases, the bonds between Cu particles were weakened and consequently allowed the grains to deform. This increase is due to the stronger oscillation of atomic bonds at higher temperatures and the asymmetric nature of the bond potential curves. Moreover, the internal thermal stresses increase with increasing temperature until reaching the material yield strength, which leads to plastic deformation of the samples [56]. This deformation occurred due to free-electron excitation during the temperature change. At high temperatures, this excitation is incapable of motivating the free electrons to move to higher paths. Therefore, these electrons remain in their original paths, which results in a similar effect on the TEC values.

In addition, Figure 8 shows the decrease in the TEC with the increasing Al₂O₃ content at the same temperature. This decrease is due to the existence of Al₂O₃ nanoparticles at the grain boundaries of the Cu matrix. Further, the good interfacial bonding between the Al₂O₃ and the Cu may participate in this decrease in TEC. Another reason for the decrease in TEC is the heat-induced thermal stresses of Cu-Al₂O₃ nanocomposites. As the temperature increases, tensile stresses increase in Al₂O₃ whilst the Cu particles are subjected to compression stress due to the difference in their own thermal expansion coefficients [56].

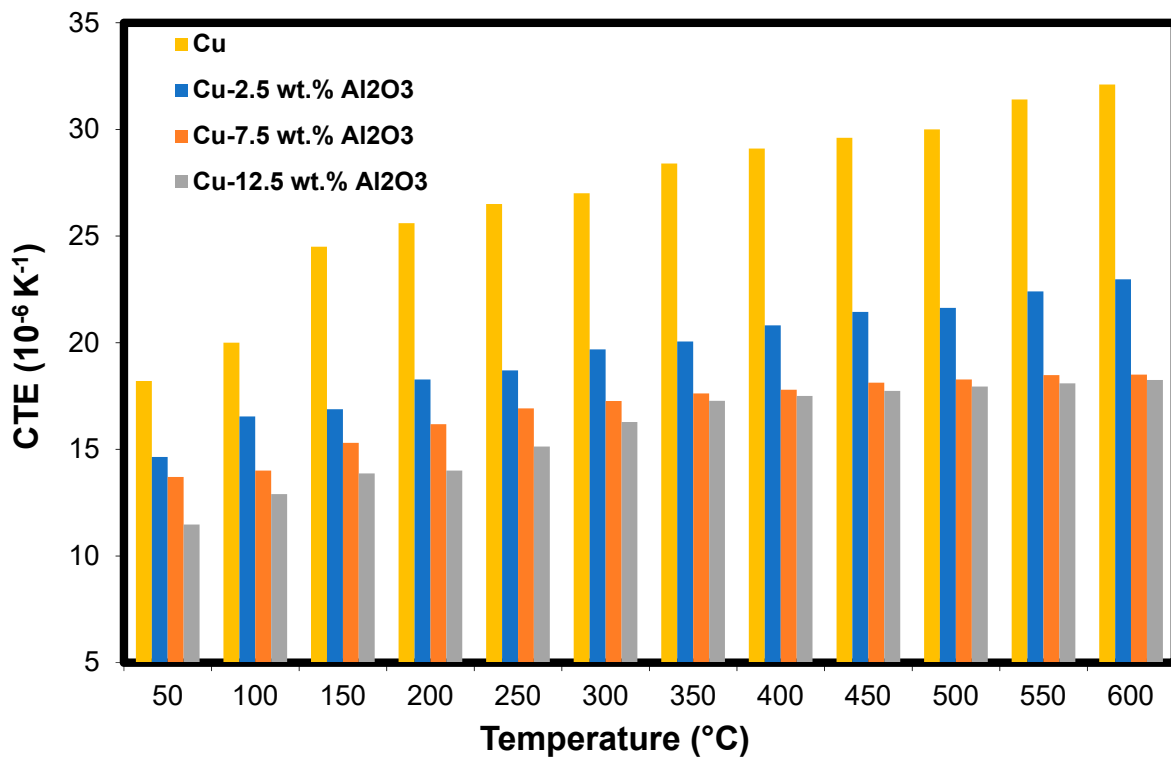


Figure 8. The coefficient of thermal expansion of the Cu-Al₂O₃ nanocomposites as a function of temperature.

4.2. Prediction of Coefficient of Thermal Expansion

A comparison between the presented LSTM-DMO and the traditional LSTM is given in Table 1 and Figure 9. It can be noted from these results that the performance of LSTM-DMO is better than the traditional LSTM in both training and testing. For example, the R² of LSTM-DMO is better than LSTM with a difference of approximately 6% in the case of the testing set, whereas the RMSE of LSTM is higher than LSTM-DMO with nearly 0.0955 and 3.0220 in training and testing stages, respectively. In the case of MAE, LSTM has a higher value than LSTM-DMO with nearly 0.0303 and 2.5280 in training and testing stages, respectively. For further analysis of the results, we use QQ plots to describe the correlation between the output and its predicted value, as shown in Figure 9. From this figure, we can observe that the developed LSTM-DMO is fitter than LSTM since the data are allocated around the straight line during the testing set.

Table 1. Results of LSTM-DMO and LSTM models.

	Training Set		Testing Set	
	LSTM	LSTM-DMO	LSTM	LSTM-DMO
R ²	0.9999	1.0000	0.936	0.995
RMSE	0.1817	0.0862	4.186	1.164
MAE	0.0515	0.0212	3.534	1.006

In addition, Table 2 illustrates the influence of changing the parameters of DMO on the performance of prediction. We assess two parameters, namely the Babysitter Exchange Parameter (*L*) and Peep, and we use three different values for each of them, and one parameter is changed the second one is fixed. In the case of changing the value of *L*, it can be noted that increasing the value of *L* from 0.6 to 0.9 at a fixed peep of 2 leads to enhancing the results of the testing set but with only a slight difference. In contrast, the performance of LSTM-DMO is slightly decreased when changing the value of *L* from 0.6 to 0.3. Moreover, when changing peep from 2 to 4 with a fixed *L* = 0.6, it can be seen that the performance is

increased, but upon decreasing the value of *peep* from 2 to 1, the prediction performance is slightly decreased.

From the above discussion, one can note the strong ability of the developed LSTM-DMO to improve the prediction of thermal expansion of Cu-Al₂O₃ nanocomposites. This results from the use of DMO, which has the ability to balance exploration and exploitation, which leads to determining the optimal parameters of LSTM. With these advantages, it has been noted that the main limitation of the proposed model is that it requires more CPU time to find the optimal solution (parameter of LSTM). In contrast, the traditional LSTM requires the shortest CPU time since it depends on one configuration of the parameters. For example, if we assumed LSTM requires K (second) during the prediction process, the developed method requires K (second) × No. (solutions) × No. (iterations).

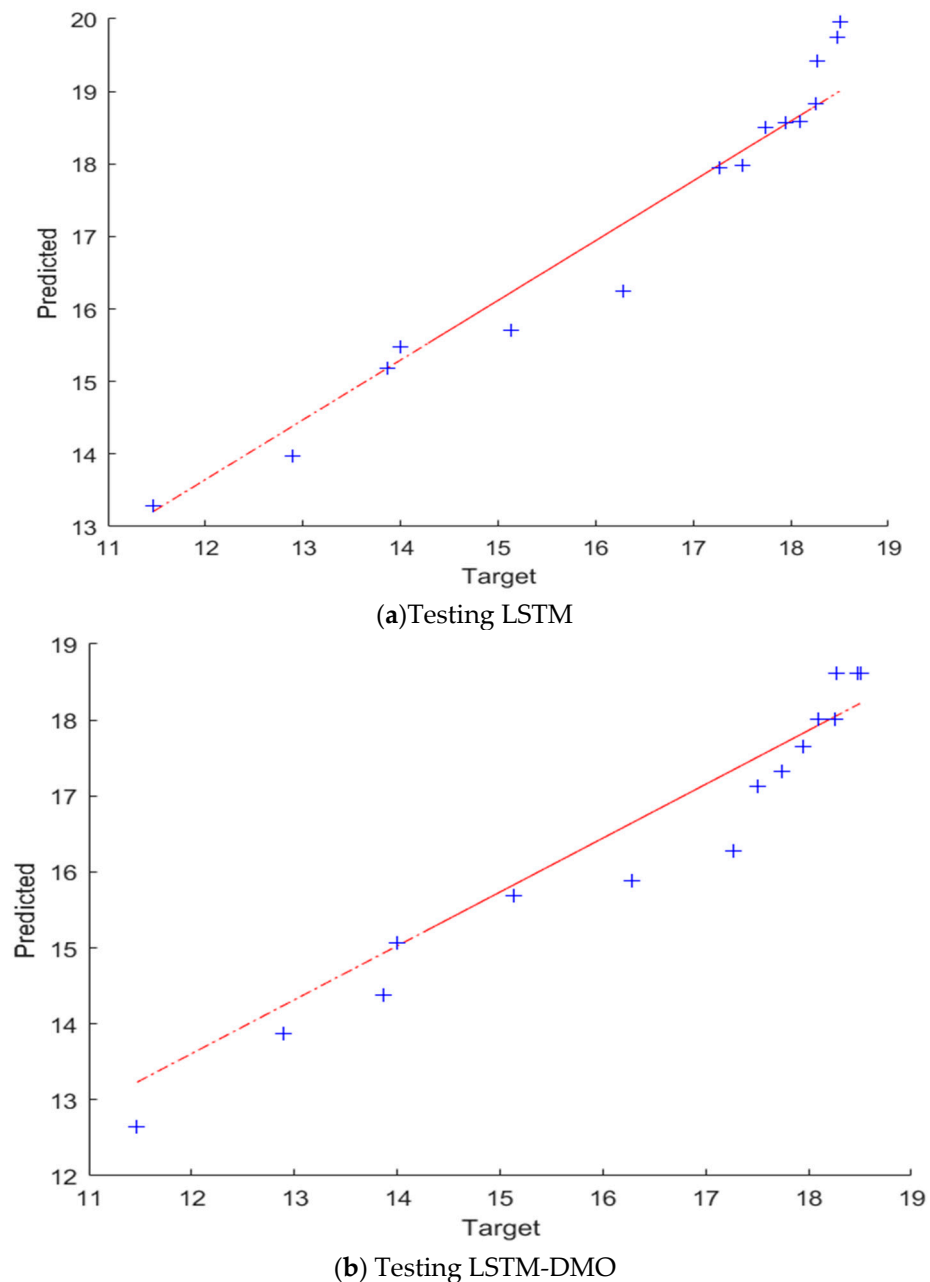


Figure 9. The QQ plots of the TEC and its prediction using LSTM, and LSTM-DMO. The predicted and target values refer to the model prediction and the experimental results of the coefficient of thermal expansion of Cu-Al₂O₃ nanocomposites.

Table 2. Influence of changing the parameters of DMO.

Parameter	$L = 0.6$		$L = 0.3$		$L = 0.9$		
	Set	Test	Train	Test	Train	Test	Train
R^2		0.995	1.0000	0.9907	0.9966	0.9988	0.9963
RMSE		1.164	0.0862	1.788	1.2934	0.5779	1.3338
MAE		1.006	0.0212	1.6014	0.8319	0.5084	0.9179
Parameter	$peep = 2$		$peep = 4$		$peep = 1$		
	Set	Test	Train	Test	Train	Test	Train
R^2		0.995	1.0000	0.9985	0.9974	0.9904	0.9948
RMSE		1.164	0.0862	0.6501	1.1348	1.8408	1.5919
MAE		1.006	0.0212	0.5896	0.6485	1.5992	1.0844

5. Conclusions

An enhanced machine learning model based on a long short-term memory algorithm was developed in this work to predict the coefficient of thermal expansion of Cu-Al₂O₃ nanocomposites with different Al₂O₃ content and was tested at different temperatures. An in situ chemical reaction method was used to produce Cu-Al₂O₃ nanocomposites with good Al₂O₃ nanoparticle dispersion. The produced samples were tested to characterize their microstructure, electrical, and thermal properties. The results showed decreases in the TEC with an increasing Al₂O₃ content at the same temperature. This decrease is due to the existence of Al₂O₃ nanoparticles at the grain boundaries of the Cu matrix. Further, the good interfacial bonding between Al₂O₃ and Cu may participate in this decrease in TEC. Another reason behind the decrease in the TEC is the heat-induced thermal stresses of Cu-Al₂O₃ nanocomposites.

The developed machine learning model was based on the modification of the long short-term memory algorithm by Dwarf Mongoose Optimization. The results showed that the model was able to predict the TEC of all the produced composites with different Al₂O₃ content, tested at different temperatures. The accuracy of the proposed model was checked using R^2 and RMSE, which reflect more than 99% accuracy of the proposed model.

Author Contributions: A.M.S., project administration, funding acquisition, data curation; I.R.N., software, validation, formal analysis, investigation; G.S.A., formal analysis, investigation; A.W., software, visualization, data curation, review and editing; M.A.E., conceptualization, methodology, formal analysis. All authors have read and agreed to the published version of the manuscript.

Funding: The authors extend their appreciation to the Deputyship for Research & Innovation, Ministry of Education in Saudi Arabia for funding this research work through the project number (IFPRC-015-135-2020) and King Abdulaziz University, DSR, Jeddah, Saudi Arabia.

Institutional Review Board Statement: Not applicable.

Informed Consent Statement: Not applicable.

Data Availability Statement: Not applicable.

Conflicts of Interest: The authors declare no conflict of interest.

Appendix A

Algorithm A1

Set the parameters of the algorithm:

Generate

For iter=1: max_iter

 Compute the fitness of the mongoose

 Set time counter C

 Determine the alpha using Equation (8)

$$\alpha = \frac{fit_i}{\sum_{i=1}^n fit_i}$$

 obtain a candidate food position utilizing Equation (9)

$$X_{i+1} = X_i + phi * peep$$

 Estimate new fitness of X_{i+1}

 Estimate sleeping mound using Equation (10)

$$sm_i = \frac{fit_{i+1} - fit_i}{\max\{|fit_{i+1}, fit_i\}}$$

 Calculate the sleeping mound average value obtained using Equation (11).

$$\varphi = \frac{\sum_{i=1}^n sm_i}{n}$$

 Compute the movement vector using

$$\vec{M} = \sum_{i=1}^n \frac{X_i \times sm_i}{X_i}$$

 Exchange babysitters if $C \geq L$, and set

 Set bs position (Equation (7)) and compute fitness

$$fit_i \leq \alpha$$

 Simulate the scout mongoose next position based on Equation (12).

$$X_{i+1} = \begin{cases} X_i - CF * rand * [X_i - \vec{M}] & \text{if } \varphi_{i+1} > \varphi_i \text{ Exploration} \\ X_i + CF * rand * [X_i - \vec{M}] & \text{else Exploitation} \end{cases}$$

 Modernize best solution so far

End For

Return best solution

End

References

1. Casati, R.; Vedani, M. Metal Matrix Composites Reinforced by Nano-Particles—A Review. *Metals* **2014**, *4*, 65–83. [\[CrossRef\]](#)
2. Kannan, C.; Ramanujam, R. Comparative study on the mechanical and microstructural characterization of AA 7075 nano and hybrid nanocomposites produced by stir and squeeze casting. *J. Adv. Res.* **2017**, *8*, 309–319. [\[CrossRef\]](#) [\[PubMed\]](#)
3. Karabacak, A.H.; Çanakçı, A.; Erdemir, F.; Özkaya, S.; Çelebi, M. Effect of different reinforcement on the microstructure and mechanical properties of AA2024-based metal matrix nanocomposites. *Int. J. Mater. Res.* **2020**, *111*, 416–423. [\[CrossRef\]](#)
4. Sadoun, A.M.; Najjar, I.M.R.; Abd-Elwahed, M.S.; Meselhy, A. Experimental study on properties of Al–Al₂O₃ nanocomposite hybridized by graphene nanosheets. *J. Mater. Res. Technol.* **2020**, *9*, 1470814717. [\[CrossRef\]](#)
5. Varol, T.; Canakci, A. Microstructure, electrical conductivity and hardness of multilayer graphene/Copper nanocomposites synthesized by flake powder metallurgy. *Met. Mater. Int.* **2015**, *21*, 704–712. [\[CrossRef\]](#)
6. Samal, C.; Parihar, J.; Chaira, D. The effect of milling and sintering techniques on mechanical properties of Cu–graphite metal matrix composite prepared by powder metallurgy route. *J. Alloys Compd.* **2013**, *569*, 95–101. [\[CrossRef\]](#)
7. Abu-Oqail, A.; Ghanim, M.; El-Sheikh, M.; El-Nikhaily, A. Effects of processing parameters of tungsten–copper composites. *Int. J. Refract. Met. Hard Mater.* **2012**, *35*, 207–212. [\[CrossRef\]](#)
8. Vettivel, S.; Selvakumar, N.; Leema, N.; Lenin, A. Electrical resistivity, wear map and modeling of extruded tungsten reinforced copper composite. *J. Mater. Des.* **2014**, *56*, 791–806. [\[CrossRef\]](#)
9. Fathy, A.; Elkady, O.; Abu-Oqail, A. Synthesis and characterization of Cu-ZrO₂ nanocomposite produced by thermochemical process. *J. Alloys Compd.* **2017**, *719*, 411–419. [\[CrossRef\]](#)
10. Fathy, A.; Wagih, A.; Abu-Oqail, A. Effect of ZrO₂ content on properties of Cu-ZrO₂ nanocomposites synthesized by optimized high energy ball milling. *J. Ceram. Int.* **2019**, *45*, 2319–2329. [\[CrossRef\]](#)
11. Zhang, X.; Lin, C.; Cui, S.; Li, Z. Characteristics of Nano-alumina Particles Dispersion Strengthened Copper Fabricated by Reaction Synthesis. *Rare Met. Mater. Eng.* **2016**, *45*, 893–896. [\[CrossRef\]](#)
12. Tjong, S.; Lau, K. Tribological behaviour of SiC particle-reinforced copper matrix composites. *Mater. Lett.* **2000**, *43*, 274–280. [\[CrossRef\]](#)

13. Guobin, L.; Jibing, S.; Quanmei, G.; Ru, W. Fabrication of the nanometer Al₂O₃/Cu composite by internal oxidation. *J. Mater. Process. Technol.* **2005**, *170*, 336–340. [[CrossRef](#)]
14. Megahed, M.; Fathy, A.; Morsy, D.; Shehata, F. Mechanical Performance of glass/epoxy composites enhanced by micro-and nanosized aluminum particles. *J. Ind. Text.* **2019**, *51*, 68–92. [[CrossRef](#)]
15. Sadoun, A.M.; Fathy, A. Experimental study on tribological properties of Cu–Al₂O₃ nanocomposite hybridized by graphene nanoplatelets. *Ceram. Int.* **2019**, *45*, 24784–24792. [[CrossRef](#)]
16. Melaibari, A.; Fathy, A.; Mansouri, M.; Eltahir, M.A. Experimental and numerical investigation on strengthening mechanisms of nanostructured Al–SiC composites. *J. Alloys Compd.* **2019**, *774*, 1123–1132. [[CrossRef](#)]
17. Sadoun, A.M.; Mohammed, M.M.; Fathy, A.; El-Kady, O.A. Effect of Al₂O₃ addition on hardness and wear behavior of Cu–Al₂O₃ electro-less coated Ag nanocomposite. *J. Mater. Res. Technol.* **2020**, *9*, 5024–5033. [[CrossRef](#)]
18. Zhang, D.; Zhan, Z. Preparation of graphene nanoplatelets-copper composites by a modified semi-powder method and their mechanical properties. *J. Alloys Compd.* **2016**, *658*, 663–671. [[CrossRef](#)]
19. Chu, K.; Jia, C. Enhanced strength in bulk graphene-copper composites. *Phys. Status Solidi A* **2014**, *211*, 184–190. [[CrossRef](#)]
20. Fathy, A.; Elkady, O.; Abu-Oqail, A. Microstructure, mechanical and wear properties of Cu–ZrO₂ nanocomposites. *Mater. Sci. Technol.* **2017**, *33*, 2138–2146. [[CrossRef](#)]
21. Abd-Elwahed, M.S.; Ibrahim, A.F.; Reda, M.M. Effects of ZrO₂ nanoparticle content on microstructure and wear behavior of titanium matrix composite. *J. Mater. Res. Technol.* **2020**, *9*, 8528–8534. [[CrossRef](#)]
22. Abu-Oqail, A.A.; Wagih, A.; Fathy, O.; Elkady, A.; Kabeel, M. Effect of high energy ball milling on strengthening of Cu–ZrO₂ nanocomposites. *Ceram. Int.* **2019**, *45*, 5866–5875. [[CrossRef](#)]
23. Fathy, A. Investigation on microstructure and properties of Cu–ZrO₂ nanocomposites synthesized by in situ processing. *Mater. Lett.* **2018**, *213*, 95–99. [[CrossRef](#)]
24. Goli, P.; Ning, H.; Li, X.; Lu, C.Y.; Novoselov, K.S. Balandin, thermal properties of graphene-copper-graphene heterogeneous films. *Nano Lett.* **2014**, *14*, 1497–1503. [[CrossRef](#)]
25. Wagih, A.; Abu-Oqail, A.; Fathy, A. Effect of GNPs content on thermal and mechanical properties of a novel hybrid Cu–Al₂O₃/GNPs coated Ag nanocomposite. *Ceram. Int.* **2019**, *45*, 1115–1124. [[CrossRef](#)]
26. Allahkaram, S.R.; Golroh, S.; Mohammadalipour, M. Properties of Al₂O₃ nano-particle reinforced copper matrix composite coatings prepared by pulse and direct current electroplating. *Mater. Des.* **2011**, *32*, 4478–4484. [[CrossRef](#)]
27. Tey, E.; Hashim, M.; Ismail, I. Characterization of Cu–Al₂O₃ and Ni–Al₂O₃ nanocomposites electrodeposited on copper substrate. *Mater. Sci. Forum* **2016**, *846*, 471–478. [[CrossRef](#)]
28. Shehata, F.; Abdelhameed, M.; Fathy, A.; Elmahdy, M. Preparation and Characteristics of Cu–Al₂O₃ Nanocomposite. *Open J. Met.* **2011**, *1*, 25–33. [[CrossRef](#)]
29. Lajevardi, S.; Shahrabi, T.; Szpunar, J. Synthesis of functionally graded nano Al₂O₃–Ni composite coating by pulse electrodeposition. *Appl. Surf. Sci.* **2013**, *279*, 180–188. [[CrossRef](#)]
30. Ning, D.; Zhang, A.; Murtaza, M.; Wu, H. Effect of surfactants on the electrodeposition of Cu–TiO₂ composite coatings prepared by jet electrodeposition. *J. Alloys Compd.* **2019**, *777*, 1245–1250. [[CrossRef](#)]
31. Ďurišínová, K.; Ďurišin, J.; Orolínová, M. Al₂O₃-dispersion strengthened nanocrystalline copper. *Powder Metall. Prog.* **2006**, *6*, 75–80.
32. Oh, S.-T.; Sekino, T.; Niihara, K. Effect of particle size distribution and mixing homogeneity on microstructure and strength of alumina/copper composites. *Nanostruct. Mater.* **1998**, *10*, 327–332. [[CrossRef](#)]
33. Ritasalo, R.; Liua, X.; Söderberg, O.; Keski-Honkola, A.; Pitkänen, V.; Hannula, S.-P. The Microstructural Effects on the Mechanical and Thermal Properties of Pulsed Electric Current Sintered Cu–Al₂O₃ Composites. *Procedia Eng.* **2011**, *10*, 124–129. [[CrossRef](#)]
34. Zhang, X.-H.; Li, X.-X.; Chen, H.; Li, T.-B.; Su, W.; Guo, S.-D. Investigation on microstructure and properties of Cu–Al₂O₃ composites fabricated by a novel in-situ reactive synthesis. *Mater. Des.* **2016**, *92*, 58–63. [[CrossRef](#)]
35. Ramezanalizadeh, H. Fabrication and Characterization of an Al-Based Nanocomposite with High Specific Strength and Good Elongation Using Large Amount CMA Nanoparticles. *J. Alloys Compd.* **2020**, *822*, 153667. [[CrossRef](#)]
36. Dhar, S.; Jena, A.; Patnaik, S.C.; Sahoo, S.K.; Tripathy, O. A Study on Microstructure and Mechanical Properties of Aluminium Matrix Composites with Micro-Sized Iron Fillers Produced by Powder Metallurgy Route. *Mater. Today Proc.* **2020**, *33*, 5617–5622. [[CrossRef](#)]
37. Charan Nayak, K.; Kumar Pandey, A.; Date, P.P. Mechanical and Physical Characterization of Powder Metallurgy Based Aluminium Metal Matrix Hybrid Composite. *Mater. Today Proc.* **2020**, *33*, 5408–5413. [[CrossRef](#)]
38. Saber, D.; Abd El-Aziz, K.; Fathy, A. Corrosion behavior of copper–alumina nanocomposites in different corrosive media. *Int. J. Mech. Eng.* **2016**, *5*, 1–10.
39. Sadoun, A.M.; Mohammed, M.M.; Elsayed, E.M.; Meselhy, A.F.; El-Kady, O.A. Effect of nano Al₂O₃ coated Ag addition on the corrosion resistance and electrochemical behavior of Cu–Al₂O₃ nanocomposites. *J. Mater. Res. Technol.* **2020**, *9*, 4485–4493. [[CrossRef](#)]
40. Rodrigues, I.; Guedes, M.; Ferro, A. Processing of Copper-Graphite-Alumina Powders by High-Energy Milling. In Proceedings of the PM2014 World Congress, 2014 World Conference on Powder Metallurgy, Orlando, FL, USA, 18–22 May 2014.

41. Khatir, S.; Boutchicha, D.; Le Thanh, C.; Tran-Ngoc, H.; Nguyen, T.; Wahab, M.A. Improved ANN technique combined with Jaya algorithm for crack identification in plates using XIGA and experimental analysis. *Theor. Appl. Fract. Mech.* **2020**, *107*, 102554. [[CrossRef](#)]
42. Zenzen, R.; Khatir, S.; Belaidi, I.; Le Thanh, C.; Wahab, M.A. A modified transmissibility indicator and Artificial Neural Network for damage identification and quantification in laminated composite structures. *Compos. Struct.* **2020**, *248*, 112497. [[CrossRef](#)]
43. Wang, S.; Wang, H.; Zhou, Y.; Liu, J.; Dai, P.; Du, X.; Wahab, M.A. Automatic laser profile recognition and fast tracking for structured light measurement using deep learning and template matching. *Measurement* **2021**, *169*, 108362. [[CrossRef](#)]
44. Fathy, A.; Megahed, A.A. Prediction of abrasive wear rate of in situ Cu–Al₂O₃ nanocomposite using artificial neural networks. *Int. J. Adv. Manuf. Technol.* **2012**, *62*, 953–963. [[CrossRef](#)]
45. Raymond, S. *Physics for Scientists and Engineers with Modern Physics*, 3rd ed.; Saunders College Publishing: Forth Worth, TX, USA, 1983.
46. Najjar, I.; Sadoun, A.; Alsuruji, G.S.; Elaziz, M.A.; Wagih, A. Predicting the mechanical properties of Cu–Al₂O₃ nanocomposites using machine learning and finite element simulation of indentation experiments. *Ceram. Int.* **2021**, *48*, 7748–7758. [[CrossRef](#)]
47. Torabi, H.; Arghavanian, R. Investigations on the corrosion resistance and microhardness of Cu–10Sn/SiC composite manufactured by powder metallurgy process. *J. Alloys Compd.* **2019**, *806*, 99–105. [[CrossRef](#)]
48. Abd-Elwahed, M.S.; Meselhy, A.F. Experimental investigation on the mechanical, structural and thermal properties of Cu–ZrO₂ nanocomposites hybridized by graphene nanoplatelets. *Ceram. Int.* **2020**, *46*, 9198–9206. [[CrossRef](#)]
49. Eltahir, M.; Wagih, A.; Melaibari, A.; Fathy, A.; Lubineau, G. Effect of Al₂O₃ particles on mechanical and tribological properties of Al–Mg dual-matrix nanocomposites. *Ceram. Int.* **2020**, *46*, 5779–5787. [[CrossRef](#)]
50. Barakat, W.; Wagih, A.; Elkady, O.A.; Abuqail, A.; Fathy, A.; El-Nikhaily, A. Effect of Al₂O₃ nanoparticles content and compaction temperature on properties of Al–Al₂O₃ coated Cu nanocomposites. *Compos. Part B Eng.* **2019**, *175*, 107140. [[CrossRef](#)]
51. Shehata, F.; Fathy, A.; Abdelhameed, M.; Moustafa, S. Fabrication of copper–alumina nanocomposites by mechano-chemical routes. *J. Alloys Compd.* **2009**, *476*, 300–305. [[CrossRef](#)]
52. Mohamed, A.; Mohammed, M.M.; Ibrahim, A.F.; El-Kady, O.A. Effect of nano Al₂O₃ coated Ag reinforced Cu matrix nanocomposites on mechanical and tribological behavior synthesis by P/M technique. *J. Compos. Mater.* **2020**, *54*, 4921–4928. [[CrossRef](#)]
53. Wagih, A.; Fathy, A.; Sebaey, T.A. Experimental investigation on the compressibility of Al/Al₂O₃ nanocomposites. *Int. J. Mater. Prod. Technol.* **2016**, *52*, 312–332. [[CrossRef](#)]
54. El-wazery, M.; El-Desouy, A.R.; Hamed, O.A.; Fathy, A.; Mansour, N.A. Electrical and mechanical performance of zirconia-nickel functionally graded materials. *Int. J. Eng.* **2013**, *26*, 375–382. [[CrossRef](#)]
55. Hsieh, C.; Tuan, W. Thermal expansion behavior of a model ceramic–metal composite. *Mater. Sci. Eng. A* **2007**, *460–461*, 453–458. [[CrossRef](#)]
56. Weber, L.; Tavangar, R. On the influence of active element content on the thermal conductivity and thermal expansion of Cu–X (X = Cr, B) diamond composites. *Scr. Mater.* **2007**, *57*, 988–991. [[CrossRef](#)]